ADVANCED HEALTHCARE MATERIALS
www.advhealthmat.de

Ruthenium Oxide Nanozyme for Tendinopathy Treatment via Countering Ferroptosis

Chenfeng Qiao, Ziying Sun, Faheem Muhammad, Wenli Gong, Jintao Lin, Jie Lv, Xi Cheng, Yuxiang Fei, Nuo Xu, Ya Xie, Ruiyang Jiang, Chenguang Lin, Haoyu Yang, Zhongyang Lv, Zheng Wang, Yuan Liu, Zhihao Lu, Xiang Gu, Zhaofeng Zhang, Chunqing Hu, Hanwen Zhang, Jia Meng, Xiaojiang Yang, Dongquan Shi, Hui Wei,* and Nirong Bao**

The global prevalence of tendinopathy (TP) is steadily increasing, resulting in functional impairments in tendons across individuals of all ages. Excessive accumulation of reactive oxygen species (ROS) plays a pivotal role in the development of TP, which compromises tendon repair and integrity through oxidative stress. This process is often accompanied by ferroptosis—a newly recognized form of iron-dependent programmed cell death. This study explores ruthenium oxide (RuO_2) hollow nanospheres as an effective nanozyme to address oxidative damage and ferroptosis in type I collagenase-induced TP. In vitro experiments show decreased mRNA levels of inflammatory biomarkers in tenocytes, while western blot analysis and immunofluorescence reveal reduced extracellular matrix degradation after RuO_2 treatment. In the TP model, the RuO_2 nanozyme therapy and improves tendon fiber arrangement, alleviates pain, and increases type I collagen expression while preventing matrix degradation. These findings suggest that the RuO_2 nanozyme possesses significant antioxidant and anti-inflammatory properties, providing protective effects on tenocytes by ROS scavenging and countering ferroptosis, indicating its potential for treating TP.

1. Introduction

Tendinopathy (TP) has become a prevalent musculoskeletal disorder, characterized by tendon swelling, pain, and functional impairment.[1] The global incidence of TP is rising. The incidence of lower limb TP is reported to be 10.52 per 1000 person-years.[2] The most commonly affected sites include the Achilles tendon, rotator cuff, and patellar tendon.[3–5] TP lesions affect both tenocytes and the collagen matrix, leading to disorganized collagen fiber alignment, disrupted extracellular matrix homeostasis, increased microvascularity, and elevated inflammation.[6] Current clinical management strategies for TP mainly include physical therapy, pharmacological treatments, loading exercises, and surgical intervention.[7] However, these treatment approaches often fail to restore

---

C. Qiao, C. Lin, J. Meng, X. Yang, N. Bao
Department of Orthopedics
Jinling Clinical Medical College
Nanjing University of Chinese Medicine
Nanjing, Jiangsu 210002, P. R. China
E-mail: bao.nirong@nju.edu.cn

Z. Sun, J. Lin, X. Cheng, Z. Lv, J. Meng, X. Yang, N. Bao
Department of Orthopedics
Nanjing Jinling Hospital
Affiliated Hospital of Medical School
Nanjing University
Nanjing, Jiangsu 210002, P. R. China

F. Muhammad
Guangdong Key Laboratory of Biomedical Measurements and Ultrasound Imaging
School of Biomedical Engineering
Shenzhen University Medical School
Shenzhen University
Shenzhen 518060, P. R. China

F. Muhammad, X. Gu, H. Wei
Department of Biomedical Engineering
College of Engineering and Applied Sciences
Nanjing National Laboratory of Microstructures
Jiangsu Key Laboratory of Artificial Functional Materials
Nanjing University
Nanjing, Jiangsu 210023, P. R. China
E-mail: weihui@nju.edu.cn

W. Gong, N. Xu, Y. Xie, R. Jiang, D. Shi
Division of Sports Medicine and Adult Reconstructive Surgery
Department of Orthopedic Surgery
Nanjing Drum Tower Hospital Clinical College of Nanjing University of Chinese Medicine
Nanjing, Jiangsu 210008, P. R. China
E-mail: shidongquan@nju.edu.cn

D. Shi
State Key Laboratory of Pharmaceutical Biotechnology
Nanjing University
Nanjing, Jiangsu 210008, P. R. China

The ORCID identification number(s) for the author(s) of this article can be found under https://doi.org/10.1002/adhm.202501035

DOI: 10.1002/adhm.202501035

Achilles tendon function to a satisfactory state. Therefore, effective treatment and further elucidation of the molecular mechanisms underlying TP are imperative. Tendon healing, particularly in cases of rupture, depends on the intrinsic responsiveness of tenocytes to surrounding stimuli, including oxidative damage and inflammatory cytokines.[8,9] Reactive oxygen species (ROS) have been implicated in oxidative stress-induced apoptotic pathways, which may contribute to the development and progression of TP.[10] In response to tissue injury, tenocytes also release pro-inflammatory cytokines like IL-1β and IL-6 to regulate extracellular matrix remodeling.[11] To counteract these harmful processes, cells rely on endogenous antioxidant defense systems, such as superoxide dismutase (SOD), glutathione peroxidase (GPx), catalase (CAT), and glutathione (GSH) to maintain cellular redox homeostasis. Significantly elevated levels of redox imbalance markers have been observed in TP tissues,[12–14] underscoring the need for effective antioxidants and ROS scavengers to clear excess ROS and alleviate inflammation.

Ferroptosis is a newly recognized form of iron-dependent programmed cell death that plays a significant role in various diseases, including TP. Distinct from apoptosis, autophagy, and necrosis, ferroptosis is characterized by lipid peroxidation, glutathione depletion, and the accumulation of ferrous ions.[15–17] Oxidative stress is a crucial factor in the initiation and progression of ferroptosis.[18] Although living organisms have evolved natural antioxidant enzymes to scavenge ROS and protect tissues from damage,[19] these enzymes often face limitations, such as instability, a lack of immune tolerance, and challenges in large-scale production.[20] Hence, there is a pressing need to develop novel nanozyme formulations to reduce oxidative damage and ferroptosis in the context of TP.

Recent advances have highlighted the enzyme-mimicking activities of various nanomaterials (i.e., nanozymes).[21] Unlike natural enzymes, these synthetic enzymes offer enhanced stability, reusability, surface functionalizability, tunable activity, and cost-effectiveness. Their activities rely on size, morphology, and external stimulation (e.g., light, sound, and heat). A diverse range of nanomaterials (e.g., CeO_2, V_2O_5, Mn_3O_4, Pt, CuSe, MoS_2 QDs, and PCN-224) have demonstrated ROS scavenging biocatalytic activities, which contribute to the protection and promotion of cell growth under oxidative stress. Among those, ruthenium-based nanozymes have been garnering a lot of attention due to their multi-enzymatic antioxidant properties.[22] Specifically, the CAT-like activity of ruthenium-based nanoformulations was found to be noticeably higher than previously reported antioxidant nanozymes.[23] In this study, we synthesized hollow RuO_2 and evaluated it as an active antioxidant nanozyme for the treatment of TP. During in vitro investigations, we observed that the RuO_2 nanozyme effectively reduced the tert-butyl hydroperoxide (TBHP)-induced oxidative homeostasis disruption and inflammation in tenocytes by counteracting ferroptosis. In vivo experimental results revealed a substantial repair of collagenase-induced TP in rats following treatment with RuO_2, thereby highlighting its therapeutic potential in promoting tendon healing.

2. Results and Discussion

2.1. Synthesis and Characterization of RuO_2 Nanospheres

A facile strategy was developed for the preparation of hollow RuO_2 nanozyme. We used cuprous oxide (Cu_2O) nanospheres as a redox reactive template to spontaneously grow an amorphous porous shell of RuO_2. Considering the toxicity of copper, in the subsequent step, the core-shelled $Cu_2O@RuO_2$ was treated with NH_4OH solution to etch the undesired Cu_2O core, resulting in the formation of hollow RuO_2 nanospheres. The synthetic protocol and the working mechanism of the hollow RuO_2 nanospheres in inhibiting oxidative stress and inflammation in tenocytes are schematically shown in **Figure 1**. Transmission electron microscope (TEM) analysis was performed to monitor the structural evolution of the Cu_2O into hollow porous structured RuO_2 nanospheres. Figure S1a (Supporting Information) shows monodispersed Cu_2O nanospheres (~200 nm); the crystalline nature of the template was verified in a high-resolution TEM image. A discrete core-shelled $Cu_2O@RuO_2$ structure can be seen in Figure S1b (Supporting Information). Lattice fringes are visible in the core region but not the outer shell, due to the amorphous nature of as-synthesized RuO_2. The inscribed circle shows the boundary between the core Cu_2O from the RuO_2 shell (the shell was ~40 nm thick). To further probe the core-shell nanostructure, high-angle annular dark-field (HAADF)–scanning transmission electron microscopy (STEM) and energy dispersive X-ray analysis (EDX) techniques were used that identified each chemical element in the core-shell morphology. Ruthenium atoms were found to be over the whole nanostructure as a shell, whereas copper signals were confined to the core region. After the dissolution of the Cu_2O core, we obtained hollow porous nanospheres of RuO_2. **Figure 2** reveals the hollow-structured RuO_2 that are mostly spherical in shape and uniform in size. In each nanosphere, the inner cavity can be readily distinguished. High-resolution TEM (HRTEM) inspection revealed that the RuO_2 shell was composed of an assembly of ultrasmall RuO_2 nanoparticles (~ 2–3 nm). The absence of lattice fringes in RuO_2 nanoparticles implied the amorphous character of ultrasmall RuO_2, randomly distributed atoms with limited ordering can be observed. The chemical composition of hollow RuO_2 nanospheres was observed by EDX mapping. The color-coded image illustrated that the interior of the particles was empty while the shell was composed of ruthenium (green) and oxygen (blue). The unique porous hollow structure of the obtained RuO_2 offers more biocatalytic active sites and ensures efficient mass transfer in nanozymatic applications. The phase composition of RuO_2 nanospheres was also measured by X-ray powder diffraction (XRD). As shown in **Figure 3a**, a disordered, nanocrystalline structure of RuO_2 nanospheres was noticed in the form of very broad peaks. The XRD findings were consistent with the HRTEM result.

J. Lv, Y. Fei, Z. Wang, Y. Liu, Z. Lu, Z. Zhang, C. Hu, H. Zhang, D. Shi
Division of Sports Medicine and Adult Reconstructive Surgery
Department of Orthopedic Surgery
Nanjing Drum Tower Hospital
Affiliated Hospital of Medical School
Nanjing University
Nanjing, Jiangsu 210008, P. R. China
H. Yang
Wuxi 9th People's Hospital affiliated to Soochow University
Wuxi, Jiangsu 214000, P. R. China

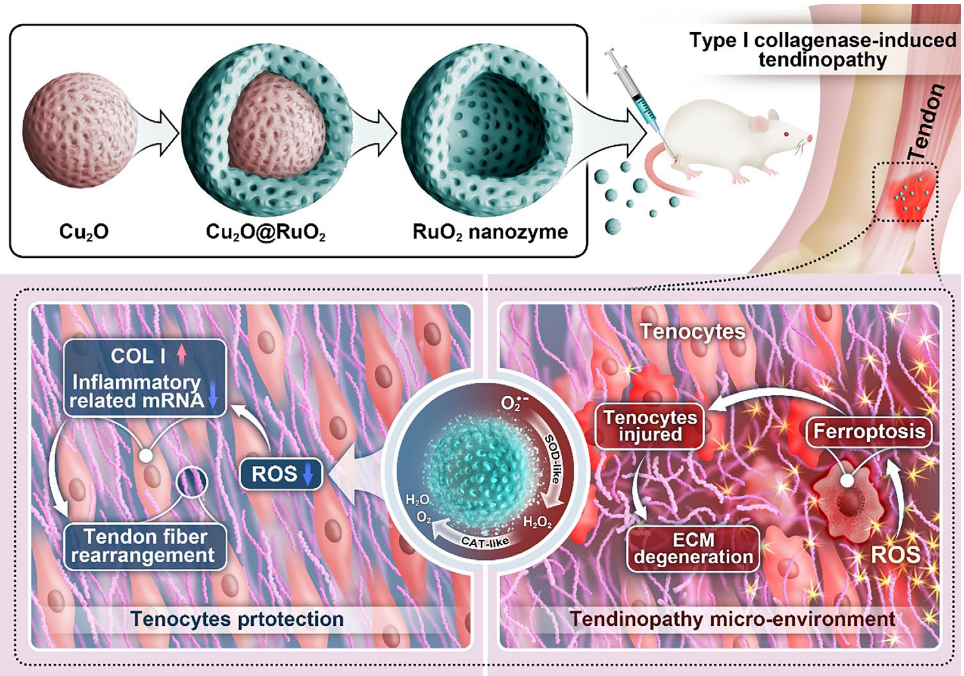

Figure 1. Schematic illustrations of RuO$_2$ nanozyme synthesis, inhibition of oxidative stress, and antagonizing ferroptosis.

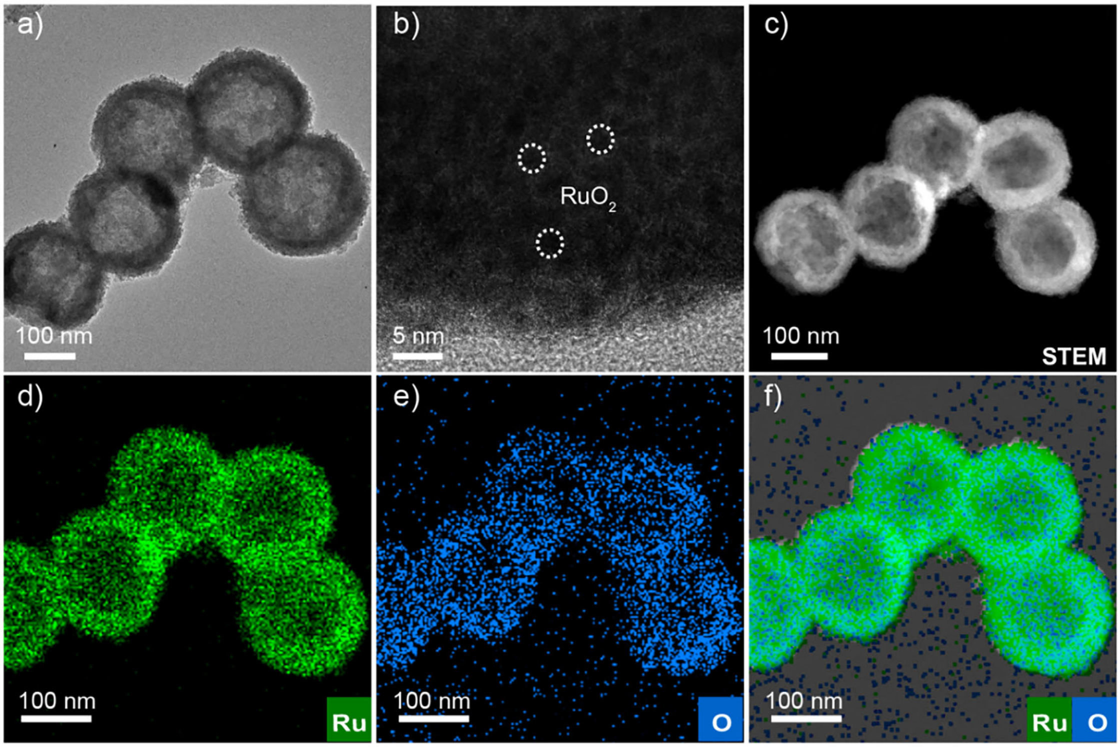

Figure 2. Electron microscopic characterization of RuO$_2$ hollow nanospheres. a) TEM; b) HRTEM; c) STEM; d–f) EDX elemental mapping images of d) Ru, e) O, f) Ru and O overlay for RuO$_2$ hollow nanospheres.

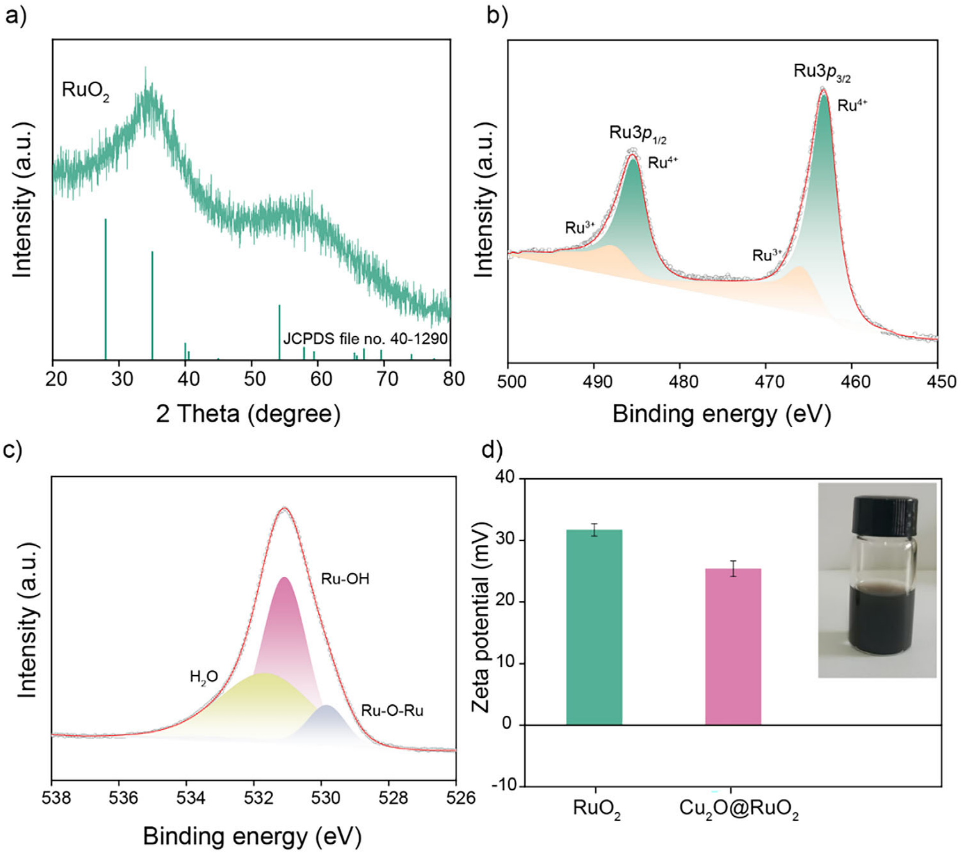

Figure 3. Structural characterization of hollow RuO_2 nanospheres. a) Powder XRD of hollow RuO_2 nanospheres. b,c) High-resolution XPS spectra of Ru 3*p* and O 1*s* in RuO_2 nanospheres. d) Zeta potentials of $Cu_2O@RuO_2$, and hollow RuO_2 nanospheres (inset: the digital photo demonstrates the colloidal stability and water dispersibility of PVP-capped RuO_2 hollow nanospheres).

To probe the surface of a RuO_2 nanosphere, X-ray photoelectron spectroscopy (XPS) was performed. Due to the overlap of the Ru 3*d* and C 1*s* peaks ≈285 eV, it is hard to investigate the presence of Ru. Hence, we analyzed XPS spectra in the Ru 3*p* region. The high-resolution Ru 3*p* XPS spectrum of RuO_2 is presented in Figure 3b showing four peaks. Two of those (463.3 and 485.5 eV) corresponded to Ru^{4+} state, whereas the remaining two (465.2 and 487.3 eV) were associated with Ru^{3+}. The deconvoluted spectrum of O 1*s* showed three noticeable peaks that could be ascribed to lattice oxygen, hydroxyl groups, and confined water content, as shown in Figure 3c.[24] The XPS results suggested that our RuO_2 product is composed of an appreciable content of trivalent hydrated portion (Ru-O-H). The synthesis of the starting Cu_2O template was carried out in the presence of a surface modifier polyvinylpyrrolidone (PVP) to ensure colloidal stability. Zeta potentials (ζ) of nanostructures involved in the synthesis of hollow RuO_2 are shown in Figure 3d. Core-shelled $Cu_2O@RuO_2$ and hollow RuO_2 showed positive ζ potential values, implying the presence of Ru^{3+} species. The digital photo in the inset specifies well-dispersed PVP-capped hollow RuO_2 nanospheres.

In addition, the hydrodynamic size of RuO_2 over different periods (0, 6, 24 h) was investigated (Figure S2, Supporting Information). The results demonstrated that PVP-capped RuO_2 hollow nanospheres exhibited a relatively uniform size distribution with a hydrodynamic diameter of ≈400 nm while maintaining a low polymer dispersion index (PDI) of 0.160. As shown in Figure S3 (Supporting Information), the Fourier transform infrared spectroscopy (FTIR) spectrum indicated that the hollow RuO_2 end product retained the surface bound-PVP, and different PVP-associated peaks appeared in the spectrum. To analyze the surface area of hollow RuO_2 nanospheres, nitrogen adsorption-desorption isotherms were recorded, showing a typical curve of a type IV isotherm with a hysteresis loop in the high relative pressure range (0.5 to 0.8). A significantly high specific surface area (Brunauer–Emmett–Teller, BET) of up to 183.9 $m^2\ g^{-1}$ was observed, which was mainly derived from the hollow and mesoporous structure (Figure S4, Supporting Information).

2.2. Enzyme-Mimicking Activities and in Vitro ROS Scavenging Ability of RuO_2

The elimination of ROS is a crucial attribute for the application of biomaterials in the treatment of ROS-associated diseases.[25] We examined the biocatalytic activities of hollow RuO_2 against various ROS. Scavenging of superoxide radicals ($O_2^{\bullet -}$) was detected using the WST-1 assay kit. We noticed a dose-dependent SOD-like activity, a progressive increase in the concentration of RuO_2 led to the corresponding quenching of $O_2^{\bullet -}$, ≈50% of radicals being scavenged when as low as 25 μg mL^{-1} of RuO_2 was exposed

(Figure S5a, Supporting Information). CAT-like nanozymes catalyze the breakdown of H_2O_2 into non-lethal H_2O and O_2, which is a crucial step in interrupting the ROS generation cascade process. We utilized a dissolved oxygen meter to quantify the CAT-like activity of RuO_2 nanospheres. As depicted in Figure S6a (Supporting Information), porous hollow RuO_2 displayed remarkably high CAT-like activity. Very low concentration of RuO_2 (1 μg mL^{-1} in 6 mL 5 mM H_2O_2) generated 25 mg L^{-1} oxygen in 5 min. Hydroxyl radical ($^{\bullet}OH$) is considered one of the most aggressive free radicals due to its high positive redox potential (2.73 V vs RHE), causing intracellular oxidative stress mutating the DNA structure, and leading to apoptosis. The $^{\bullet}OH$ scavenging ability of RuO_2 was assessed using the $^{\bullet}OH$-assay kit (that works on the classical Fenton reaction principle). As shown in Figure S7 (Supporting Information), the escalating RuO_2 concentrations correlated with the quenching of $^{\bullet}OH$, indicating a dose-dependent $^{\bullet}OH$ scavenging effect. To provide a comparison, we also assessed the ROS scavenging activities of four previously reported antioxidant nanozymes: CeO_2, Mn_3O_4, Co_3O_4, and Cu_2O. As illustrated in Figure S5b–e (Supporting Information), the SOD-like activity of RuO_2 was found to be comparable to that of CeO_2 and Co_3O_4. In contrast, Cu_2O and Mn_3O_4 exhibited relatively low ROS scavenging efficiencies. The CAT-like activities were assessed to determine the oxygen production capabilities of various nanomaterials (Figures S6b–e, Supporting Information). Hollow RuO_2 nanospheres, at a concentration of 1 μg mL^{-1}, produced almost 30 mg mL^{-1} of oxygen in just 5 min, which increased to 40 mg mL^{-1} at 2 μg mL^{-1}. In contrast, CeO_2 and Co_3O_4 generated less than 9 mg mL^{-1} of oxygen under the same conditions, while Mn_3O_4 and Cu_2O produced below 15 mg mL^{-1}. Overall, the oxygen production efficiency of CeO_2, Mn_3O_4, Co_3O_4, and Cu_2O was significantly lower than that of RuO_2. This indicates that RuO_2 emerged as a superior option for enhanced antioxidant therapies.

2.3. Protective Effects of RuO_2 Nanozyme Against TBHP-Induced Oxidative Stress and Inflammatory Response in Tenocytes

The biocompatibility, antioxidant, and anti-inflammatory properties of RuO_2 nanozyme were investigated at the cellular level. The results demonstrated the biocompatibility and nontoxic features of RuO_2 when the concentration was kept below 20 μg mL^{-1}. No significant differences in the viability or cytoskeletal morphology of treated tenocytes compared to untreated cells were observed, as shown by calcein acetoxymethyl ester/propidium iodide double staining (AM/PI) and phalloidin staining. However, manifested cytoskeletal shrinkage at a concentration of 50 μg mL^{-1}, yet the cell count did not exhibit any significant reduction (Figure S8a,b,e, Supporting Information). Further analysis using the Cell Counting Kit (CCK)-8 assay confirmed that tenocytes viability was not significantly affected when RuO_2 concentration was below 10 μg mL^{-1} (Figure S8g, Supporting Information). The discrepancies between the staining and CCK-8 results suggested that at higher concentrations, RuO_2 nanozyme might impair cell viability without inducing cell death. Since tendon injury involves the recruitment of immune cells and the secretion of inflammatory cytokines, which trigger an inflammatory cascade leading to tendon degeneration and calcification, the role of macrophages in TP is of particular significance.[26,27] While evaluating the biocompatibility of the RuO_2 in RAW264.7 cells, we noted results analogous to those observed with tenocytes (Figure S8c,d,f,h, Supporting Information). Additionally, histological analysis of animal tissues also revealed no significant morphological or cellular abnormalities in the heart, liver, spleen, lungs, or kidneys (Figure S9, Supporting Information), primarily confirming the biocompatibility of RuO_2 nanozyme at low doses. Biocompatibility and safety of nanomaterials are preconditions for their application in the human body, the above findings have encouraged us to further explore RuO_2 cytoprotective effects, anti-inflammatory activities, and ROS scavenging characteristics in the context of TP.

Next, the expression levels of type I collagen (Col1a1), type III collagen (Col3a1), and matrix metalloproteinase-13 (Mmp13) proteins were evaluated (**Figure** 4a). Hollow RuO_2 nanozyme was found to enhance Col1a1 expression while suppressing the expression of Col3a1 and effectively inhibiting Mmp13 expression. These findings indicate that RuO_2 nanozyme can counteract the redox imbalance induced by TBHP in tenocytes, promote the regeneration of damaged tenocytes, and prevent extracellular matrix degradation, thereby supporting TP healing. Quantitative Real Time-PCR (qPCR) results also corroborated the protein expression data, confirming that RuO_2 nanozyme was involved in early-stage protein translation to protect tenocytes from TBHP-induced oxidative damage (Figure 4e–g; Figure S10a, Supporting Information). The inflammatory response plays a crucial role in the pathological progression of TP and may impede the natural healing process of TP. We quantitatively analyzed the mRNA expression levels of the inflammatory mediators *IL-1β* and *IL-6*, and the results showed that TBHP-induced oxidative stress significantly upregulated the expression of these inflammatory factors compared to the control group. However, it was demonstrated that the treatment with RuO_2 nanozyme significantly alleviated the TBHP-induced inflammatory response (Figure 4h,i). Scleraxis (*Scx*), primarily expressed in tendons, is critical for tendon development,[28] while mohawk (*Mkx*) maintains normal tendon physiology and promotes tendon injury repair.[29] Through qPCR analysis, we found that the mRNA expression levels of *Scx* and *Mkx* were significantly upregulated after treatment with RuO_2 nanozyme (Figure 4j,k), providing important clues for understanding the pathogenesis of TP and exploring new therapeutic strategies. Immunofluorescence (IF) analysis was performed which demonstrated that TBHP treatment mitigated Col1a1 expression while increasing the Col3a1 expression, and induced morphological changes in tenocytes, all observations were reversed by RuO_2 nanozyme treatment (Figure 4l,m). Tendon tissues are characterized by a substantially higher expression level of Col1a1 compared to Col3a1, and the IF observations provided evidence that RuO_2 nanozyme enhanced the expression of Col1a1, thus improving the mechanical strength and functionality of tenocytes, as well as protecting the microenvironment of injured tenocytes.

2.4. Therapeutic Potential of RuO_2 Nanozyme in TP Models Induced by Type I Collagenase

After conducting a thorough investigation into the antioxidant and anti-inflammatory effects of RuO_2 nanozyme in tenocytes,

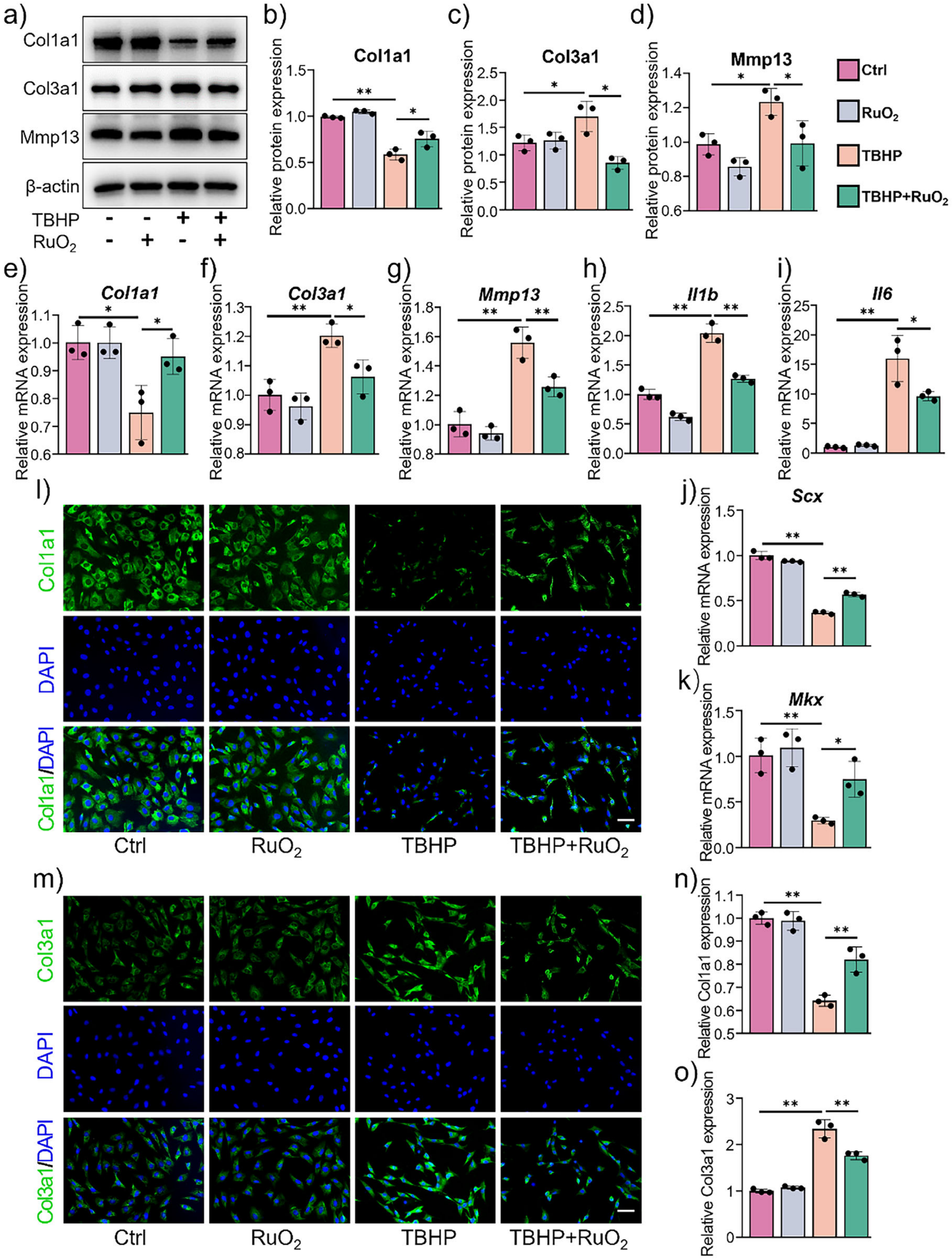

Figure 4. RuO_2 nanozyme alleviates tert-butyl hydroperoxide (TBHP)-induced oxidative stress and inflammatory response in tenocytes. a) Representative western blot image of Col1a1, Col3a1, Mmp13, and β-actin expression in tenocytes after TBHP stimulation with or without RuO_2 nanozyme treatment for 4 h. b–d) Quantification of western blot image expression of tenocytes after TBHP treatment for 4 h with or without RuO_2 nanozyme. e–k) qPCR analysis of indicated genes in tenocytes treated with TBHP with or without RuO_2 nanozyme for 4 h. l,m) Representative immunofluorescence staining of Col1a1 and Col3a1 in tenocytes after TBHP treatment with or without RuO_2 nanozyme. Scale bar: 50 µm. n,o) Quantitative analysis of (l and m). One-way analysis of variance (ANOVA) was conducted to assess the statistical differences among the means of multiple groups. Data are presented as mean ± SD, $n = 3$ independent experiments. $^*P < 0.05$, $^{**}P < 0.01$.

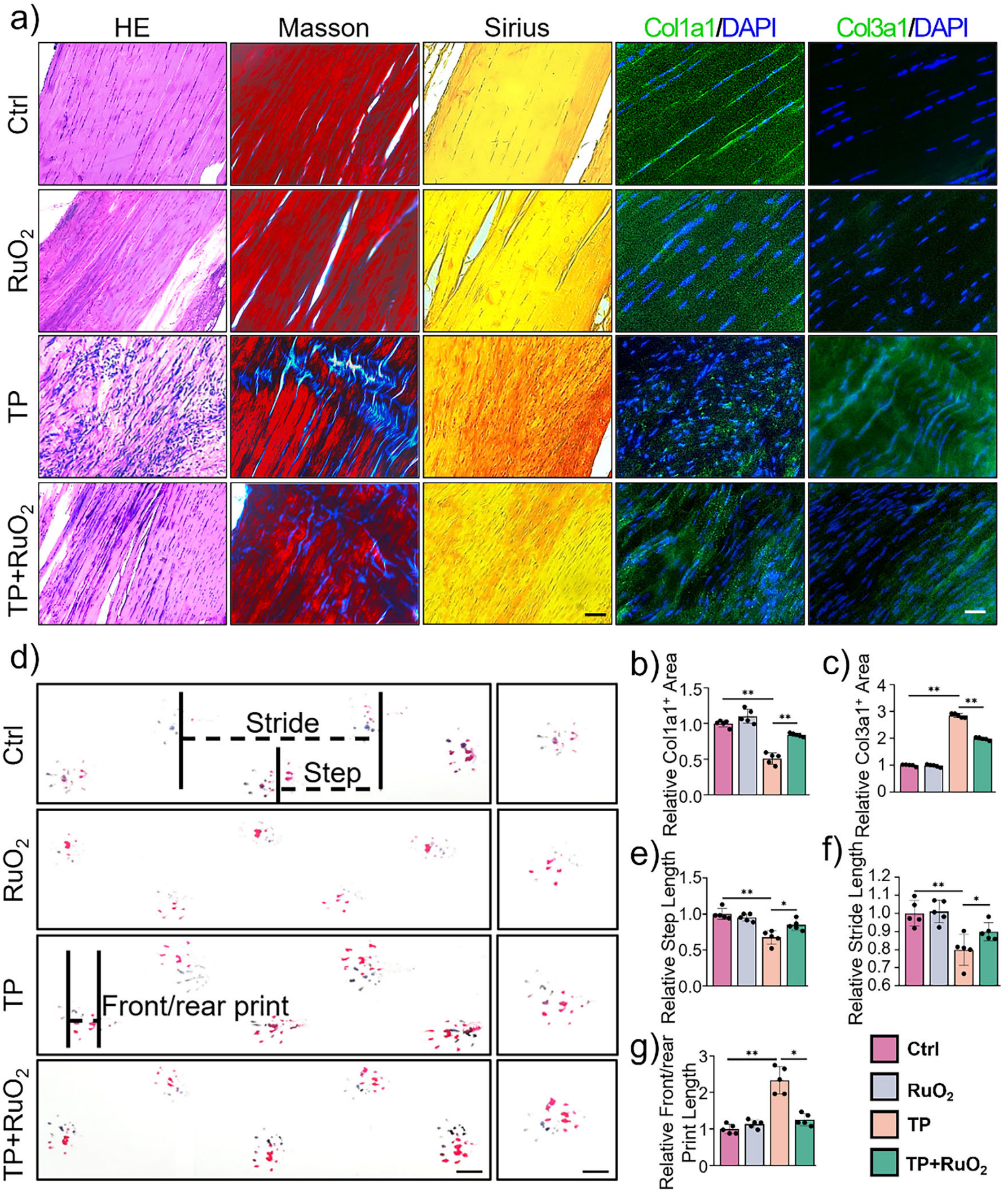

Figure 5. Evaluation of the repair effect of RuO_2 nanozyme on tendinopathy (TP) rats. a) Hematoxylin and eosin (H&E) staining, Masson's trichrome staining, Sirius Red staining, and immunofluorescence of Col1a1 and Col3a1 in the four groups (control, RuO_2 nanozyme, TP, and TP with RuO_2 nanozyme). Scale bars: 50 µm. b,c) The proportions of Col1a1 and Col3a1 positive areas in the four groups. d) Representative rat footprints in the footprint assay. Blue footprints: forelimbs; red footprints: hind limbs. Scale bars: 1.5 cm (left), 1 cm (right). e–g) The RuO_2 nanozyme treatment further increased the relative stride length and step length and reduced the relative front/rear print length in the treatment group compared to the TP treatment group. One-way ANOVA was conducted to assess the statistical differences among the means of multiple groups. Data are presented as mean ± SD, *n* = 5 independent experiments. $^{*}P < 0.05$, $^{**}P < 0.01$.

its protective efficacy was further assessed in a rat model of TP. Hematoxylin and eosin (H&E) staining revealed that compared to the control group, the TP model group displayed significant disruption in tendon structure. This disruption was characterized by increased neovascularization, inflammatory cell infiltration, and heightened cell proliferation (**Figure** 5a). Moreover, Masson's trichrome staining showed a notable increase in the formation of low-density collagen (blue) within the TP group. Notably, the injection of RuO_2 nanozyme alone did not affect the structure of normal tendon tissue. However, in the TP model, RuO_2

nanozyme significantly decreased inflammatory cell infiltration and neovascularization within the tendon, while restoring the normal histological architecture (Figure 5a). Masson's trichrome staining further demonstrated that RuO_2 nanozyme promoted the formation of high-tensile collagen fibers (red). To further validate the reparative effects of RuO_2 nanozyme, Sirius red staining and IF staining for Col1a1 and Col3a1 were conducted. Sirius red staining showed minimal expression of Col3a1 (red) on a faint yellow (Col1a1) background in the control group, while Col3a1 expression was significantly increased in the TP group (Figure 5a). Additionally, IF staining clearly highlighted the changes in the expression of Col1a1 and Col3a1. In healthy tendons, Col3a1 expression was low, whereas Col1a1 was highly expressed and organized in a structured manner (Figure 5a). In contrast, the TP group exhibited a marked increase in Col3a1 expression and a significant decrease in Col1a1 expression, accompanied by disorganized collagen arrangement. These changes were effectively reversed by RuO_2 nanozyme treatment (Figure 5a–c). Interestingly, the Sirius red staining and IF results indicated that RuO_2 nanozyme did not induce any changes in the structure of normal tendons. Moreover, to evaluate pain and gait in the rats, footprint analysis was performed. The results showed that RuO_2 treatment significantly reduced pain and improved the gait of the TP rats, as evidenced by improvements in stride length, step length, and a reduction in the distance between front and rear prints (Figure 5d–g). Treatment with RuO_2 nanozyme in the TP group led to the restoration of the disorganized and loose collagen structure to a more ordered and compact arrangement, significantly enhancing the locomotor function of TP-injured rats.

Recent advances in tendon tissue engineering have integrated electrospun nanofibrous yarn fabrication with conventional textile manufacturing to develop novel nano-micro fibrous woven scaffolds.[30] These engineered scaffolds demonstrate tendon-mimetic anisotropic architecture and high tensile strength characteristics, showing potential for addressing large-scale tendon defects. In vitro evaluations revealed that such woven matrices significantly enhance tendon cell adhesion, elongation, proliferation, and phenotypic stability. Unlike those structurally optimized nano-scaffolds, our therapeutic strategy directly targets the core pathological mechanisms of tendon degeneration through the synergistic action of RuO_2 nanozyme. The engineered RuO_2 platform demonstrates superior antioxidant capacity, and pro-regenerative bioactivity, effectively scavenging ROS, promoting collagen biosynthesis, and preventing oxidative stress-induced cellular damage and extracellular matrix (ECM) degradation. Previous investigations have documented that nanoceria exerted antioxidant and anti-inflammatory effects via NRF2 nuclear translocation mediated through ERK signaling activation, showing protective effects against tendon fiber damage in rat models.[31] Comparative analysis in our study demonstrated that RuO_2 nanoparticles exhibit significantly enhanced antioxidant performance over CeO_2 analogs. This improved therapeutic efficacy translated to better functional recovery in TP models, as evidenced by restored mobility and reduced pain responses in Achilles tendon injury models. Histopathological assessments further confirmed the superior capacity of RuO_2 in maintaining tendon microstructure and preventing degenerative changes. Overall, these findings suggest the potential therapeutic value of RuO_2 nanozyme in the treatment of TP.

2.5. RuO_2 Nanozyme Mitigate Ferroptotic Features in Tenocytes Under Oxidative Stress

Following the investigation of the therapeutic effects of RuO_2 nanozyme in a rat model of TP, the underlying mechanisms of ferroptosis in TP were further explored. Iron, as an essential trace element in the human body, participated in various physiological metabolic processes and was recycled within the body through the filtration function of the glomeruli and the reabsorption mechanism of the renal tubules. The iron metabolism process encompassed multiple steps, including intake, storage, utilization, and excretion, which were finely regulated by a series of proteins.[32] Ferroptosis is a newly recognized form of iron metabolism-dependent programmed cell death, the core features of which include the accumulation of iron ions, lipid peroxidation within cells, and the depletion of GSH. The mechanism of this cell death is distinctly different from the classical cell death pathways, such as autophagy, apoptosis, and necrosis. According to our research, iron metabolism also plays a pivotal role in TP pathogenesis (Figure S11, Supporting Information). The effects of necrosis, apoptosis, and ferroptosis on tenocytes were systematically evaluated using the CCK-8 assay. It was found that the necrosis inhibitor (Necrosulfonamide) demonstrated no rescue effect against the TBHP-induced decrease in tenocyte viability. In contrast, apoptosis inhibitors (Z-VAD-FMK), ferroptosis inhibitors (Ferrostatin-1), and RuO_2 were all capable of rescuing tenocytes viability. However, the rescue effect of Z-VAD-FMK was not statistically significant, whereas RuO_2 exhibited superior efficacy compared to Ferrostatin-1. These findings suggest that targeting ferroptosis may modulate tenocyte fate, hence the use of RuO_2 demonstrates an antagonistic effect on ferroptosis in tenocytes. IF analysis revealed that RuO_2 nanozyme significantly attenuated the ferroptotic features of TBHP-induced tenocytes, including dropped intracellular lipid peroxidation, ROS levels, and Fe^{2+} accumulation (**Figure** 6a–e).

We employed western blot techniques to deeply investigate the effects of RuO_2 nanozyme on the expression of ferroptotic proteins, aiming to reveal their role in the regulation of iron metabolism. It was found that the RuO_2 nanozyme significantly suppressed the expression of the ferroptosis driver Cox2 while promoting the expression of ferroptosis inhibitors Gpx4 and Fth1 (Figure 6f–i). qPCR further validated the influence of RuO_2 on the expression of ferroptosis-related genes, including *Ptgs2*, *Acsl4*, and *Tfrc* (Figure S10b–d, Supporting Information). The results showed that under TBHP treatment, the expression of these ferroptosis-inducing genes was markedly decreased by RuO_2 nanozyme, suggesting that nanozyme exert their protective effects in tenocytes by antagonizing ferroptosis. The burgeoning interest in ferroptosis has led to an increasing number of studies reporting on its role in disease progression and potential therapeutic applications. For instance, ferroptosis has been implicated in lung damage caused by nanoplastics,[33] and its promotion in methicillin-resistant *Staphylococcus aureus* (MRSA) has been explored as a treatment for acute pneumonia.[34] Additionally, targeting ferroptosis in hepatocellular carcinoma cells has emerged as a novel treatment strategy for liver cancer.[35] However, there is a notable scarcity of reports concerning the targeting of ferroptosis for the treatment of TP. This study aimed to provide additional therapeutic strategies for TP by exploring the role of ferroptosis in

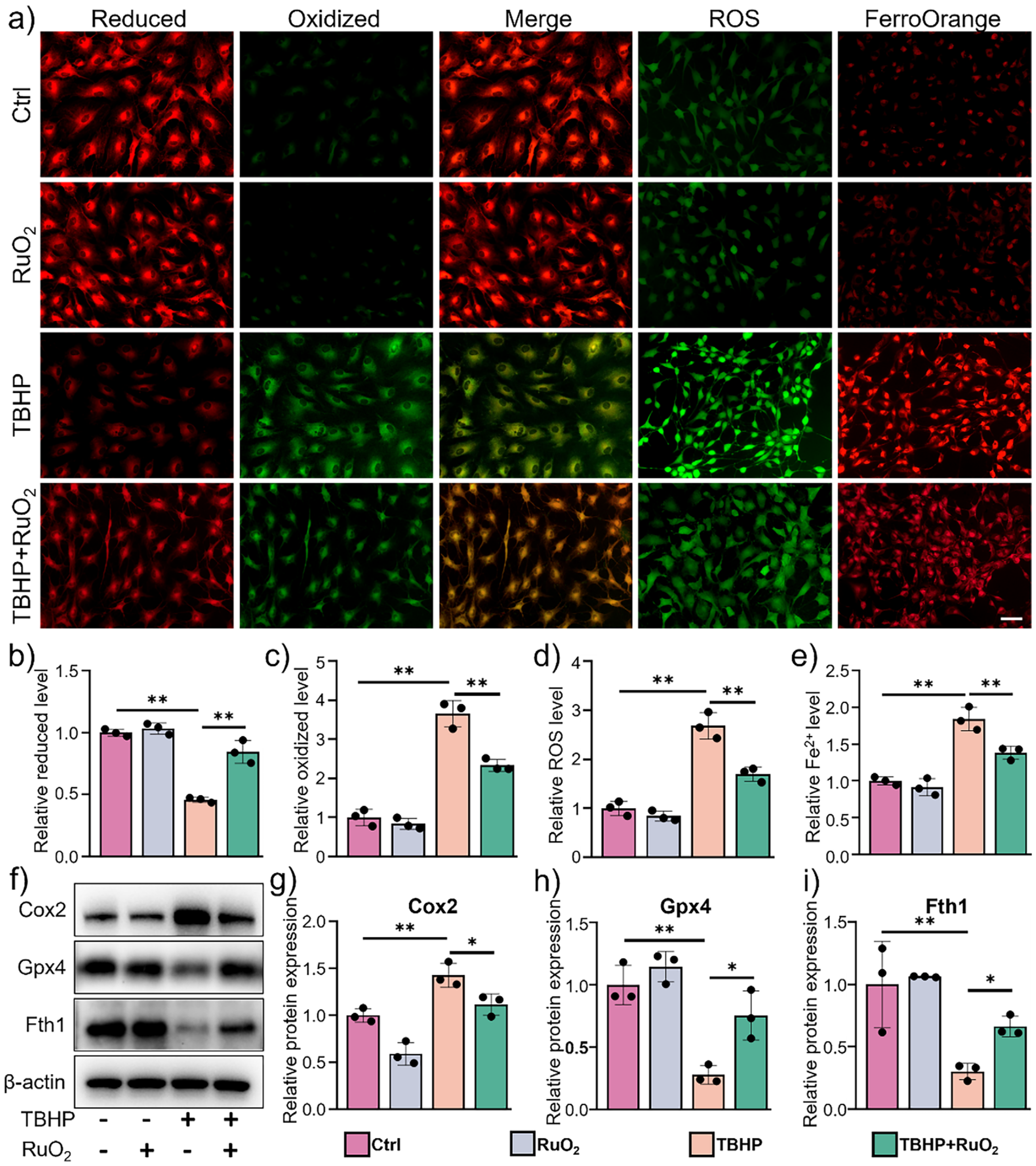

Figure 6. Evaluation of the effect of RuO_2 nanozyme on ferroptosis in TP. a) Cellular lipid peroxidation (C11BODIPY), total reactive oxygen species (ROS), and FerroOrange (Fe^{2+}) fluorescence analysis. Scale bars: 50 µm. b–e) Quantification of C11BODIPY, total ROS, and Fe^{2+} fluorescence. f) Representative western blot image of Cox2, Gpx4, Fth1, and *β*-actin expression in tenocytes after TBHP stimulation with or without RuO_2 nanozyme treatment for 4 h. g–i) Quantification of western blot image expression of tenocytes after TBHP treatment for 4 h with or without RuO_2 nanozyme. One-way ANOVA was conducted to assess the statistical differences among the means of multiple groups. Data are presented as mean ± SD, *n* = 3 independent experiments. $^{*}P < 0.05$, $^{**}P < 0.01$.

this condition. The nanozyme treatment slowed the progression of TP and suggested that RuO_2 nanozyme could also be applied to other iron-related diseases.

3. Conclusion

In summary, we presented the RuO_2 nanospheres as a potent antioxidant nanozyme that effectively alleviated type I collagenase-induced TP. In vitro studies revealed that the RuO_2 nanozyme possessed excellent ROS scavenging capabilities, and as a result, a marked reduction in extracellular matrix degradation (induced by TBHP) was observed in tenocytes. This included preserving key proteins such as Col3a1 and Mmp13; moreover, the RuO_2 nanozyme was found to promote tendon regeneration and maintain the physiological functions of tendons, as evidenced by the expression of Col1a1, the tendon-specific regulatory factors (*Scx* and *Mkx*). Notably, our findings in a rat TP model also indicated that RuO_2 nanozyme enhanced the healing process and lowered the disease progression by inhibiting the ferroptosis pathway. Overall, this report suggests that RuO_2 nanozyme offers promising potential for treating TP and provides new insights into therapies for ferroptosis-related diseases.

4. Experimental Section

Chemicals: The PVP, copper (II) nitrate trihydrate (Cu $(NO_3)_2 \cdot 3H_2O$), hydrous ruthenium (III) chloride ($RuCl_3 \cdot xH_2O$), hydrogen peroxide (H_2O_2, 30 wt.% in H_2O), ethylene glycol (EG), ammonium hydroxide (25% NH_4OH), and sodium hydroxide (NaOH) were obtained from Aladdin Chemical Co. Ltd. (Shanghai, China). The hydroxyl radical assay kit was purchased from Nanjing Jiancheng Bioengineering Institute. Deionized water (18.2 MΩ· cm, Millipore), 75% ethanol, or anhydrous ethanol were used throughout the experiments.

Material Characterizations: The structural characteristics of RuO_2 nanospheres were studied using a scanning electron microscope Ultra 55 (Zeiss, Germany) and a TEM (FEI TECNAI G2 F20 200 kV). The HAADF-STEM images with aberration correction were obtained using an FEI Themis Z instrument (Thermo Fisher Scientific) at an accelerating voltage of 300 kV. The elemental composition was determined using an inductively coupled plasma optical emission spectrometer (Avio 220 Max, PerkinElmer). The XRD pattern of RuO_2 powder was recorded using a diffractometer (Bruker-AXS, Germany) with Cu Kα radiation. The zeta potential of RuO_2 was measured using a Malvern Zetasizer Nano ZS90 at 25 °C. XPS analysis was performed using a Thermo Scientific K-Alpha spectrometer (Al Kα (1486 eV)) equipped with a hemispherical energy analyzer; the binding energies were calibrated by considering the C1s peak at 284.8 eV. The specific surface area was measured at 77 K using a Kubo X1000 (Biaode, China). FTIR analysis was performed using a Thermo Scientific Nicolet iS 5 FTIR spectrometer (USA). To determine the catalase-like activity of RuO_2, the generated oxygen (mg L^{-1}) was evaluated using a dissolved oxygen meter (SevenExcellence Multiparameter, Mettler Toledo Co. Ltd.).

Synthesis of Hollow RuO_2 Nanospheres: Cu_2O nanospheres were first prepared as a template using a previously reported method.[36] The aqueous solution of $RuCl_3 \cdot xH_2O$ (150 mg, 2 mL) was introduced into 20 mL of the as-synthesized Cu_2O nanospheres (100 mg) aqueous solution while vigorously stirring at room temperature. As a result, the spontaneous growth of ultrasmall RuO_2 nanoparticles as a shell layer was achieved. After stirring for 30 min, the precipitate was recovered by centrifugation and redispersed in 20 mL of water. The pH of the solution was adjusted to 10 by adding NaOH solution, and then 100 µL of 30% H_2O_2 was added to increase the content of Ru^{4+} in the as-synthesized RuO_2. The resulting solution was then heated at 80 °C for 30 min, and the core-shell $Cu_2O@RuO_2$ nanospheres were collected by centrifugation. In the following step, the undesired Cu_2O was etched using an ammonia solution. Nanospheres of $Cu_2O@RuO_2$ (30 mg) were dispersed in 5 mL of deionized water, and then 2 mL of 25% NH_4OH was slowly added under stirring. After 1 h of incubation in the ammonia solution, the final PVP-coated hollow RuO_2 nanospheres were collected, and washed with water and ethanol twice to remove impurities. For sterilization, 25 mg of the obtained RuO_2 nanospheres were first washed with 75% ethanol, centrifuged, and washed. The obtained powder was then dried in an oven and sterilized under UV light for 15 min. Finally, the sterilized powder was dispersed in 1 mL of sterile deionized water to prepare a 25 mg mL^{-1} RuO_2 nanozyme solution for further experiments. Other nanomaterials (i.e., CeO_2, Mn_3O_4, Co_3O_4, and Cu_2O) were synthesized using previously reported methods.[36–39]

SOD-Like Activity Measurements: The SOD-like activity of RuO_2 nanospheres was detected using a SOD assay kit (Dojindo, Japan). According to the instructions of the manufacturer, known concentrations of RuO_2 nanospheres were mixed with 200 µL of the working solution in a microplate, then 20 µL of the enzyme working solution was added and incubated the microplate in the oven at 37 °C for 20 min. The absorbance was measured at 450 nm using a microplate reader. The rate of superoxide radical quenching was determined by measuring the inhibition in the formazan generation. The analysis was performed in triplicate ($n = 3$). The SOD-like activity of CeO_2, Mn_3O_4, Co_3O_4, and Cu_2O were detected using the same methodology.

CAT-Like Activity Measurements: The CAT-like activity of RuO_2 nanospheres was evaluated by monitoring the amount of catalytically generated dissolved oxygen with an oxygen meter. Specific concentrations of RuO_2 (1 and 2 µg mL^{-1}) and H_2O_2 were added sequentially to 6 mL of water; the final H_2O_2 concentration was kept at 5 mM. The amount of oxygen (mg L^{-1}) generated by the RuO_2-mediated reaction was monitored for up to 10 min. The CAT-like activity of CeO_2, Mn_3O_4, Co_3O_4, and Cu_2O were evaluated using the same procedure.

Hydroxyl Radicals Quenching Measurements: The $^{\bullet}OH$ scavenging potential of RuO_2 nanospheres was determined using the $^{\bullet}OH$-assay kit (based on the classical Fenton reaction principle). Known concentrations (6.25, 12.5, 25, 50, and 100 µg mL^{-1}) of sterile RuO_2 were added into the pre-prepared reagent solution and chromogenic agent, and kept the samples for 20 min at room temperature. Then, the absorbance (550 nm) of the colored product was measured using a microplate reader to quantify the amount of hydroxyl radicals. To ensure accuracy, the analysis was performed in triplicate ($n = 3$).

Animal Study: Adult male Sprague–Dawley (SD) rats (250–300 g, $n = 24$) were obtained from SPF (Beijing) Biotechnology Co. Ltd. All rats were housed in a specific pathogen-free (SPF) environment at 24 °C with a 12 h light/dark cycle and had free access to food and water during the entire experimental period. Animal experiments were performed following the guidelines of the Ethics Committee of Drum Tower Hospital, Medical School of Nanjing University, Nanjing, China (Ethics approval number: 2023AE02017).

The TP model was established by injecting 50 µL of type I collagenase (5 mg mL^{-1}) into the right hindlimb of the rats. After the acclimation period, the rats were randomly divided into four groups: 1) the control group, injected with saline; 2) the RuO_2 group, injected with RuO_2 nanozyme (50 µL, 5 µg mL^{-1}); 3) TP group, injected with type I collagenase; and 4) treatment group, received a co-treatment of type I collagenase injection and RuO_2 nanozyme. Each group had 6 rats. The TP group and the treatment group received type I collagenase injections every 2 days for 2 weeks. After 2 weeks, the RuO_2 group and the treatment group received RuO_2 nanozyme injections every 2 days for another 2 weeks. The control group received saline injections for 1 month. The injection volume was 50 µL for each administration. One month later, all rats underwent a footprint analysis, and then the tendons and major organs from all groups were collected for further histological examinations.

H&E, Masson Trichrome, and Sirius Red Staining of Tendon Sections: For histological analysis, rat tendon samples were first fixed in 4% paraformaldehyde for 48 h, then dehydrated through a graded ethanol series, and finally embedded in paraffin. Sections were cut at a thickness of 4 µm. Deparaffinization and rehydration were performed before staining. Staining was conducted using an H&E staining kit (Beyotime, China), Masson's trichrome staining kit (Beyotime, China), and a Sirius red staining kit (Solarbio, China). Finally, the stained sections were observed and photographed under a bright-field microscope (ZEISS Axio Lab.A1, Germany).

Footprint Assay: A 7-day habituation period was provided before testing to lessen environmental stressors.[40] The rats' paws were color-coded with harmless dyes, with forepaws marked in blue and hind paws in red. The rats were placed in a calm and dark environment and allowed to ambulate along a 60 × 20 cm track lined with white paper. The assay was conducted in triplicate for each rat. The resulting paw prints were used to reflect the rats' locomotor function and nociceptive thresholds.

Isolation and Culture of Tenocytes: As previously described, tendon tissue was harvested from the rats for in vitro cell experiments.[31] Specifically, tendons were isolated from 2–4 weeks old male SD rats, and cleaned thoroughly using sterile PBS. The tendon tissue was then minced into 1 mm^3 fragments and digested overnight at 37 °C in a 3 mg mL^{-1} collagenase I (Gibco, USA) solution. After filtration and centrifugation, the cell pellet was resuspended in DMEM/4.5 g glucose medium (Gibco, USA) supplemented with 10% fetal bovine serum (Vazyme, China) and 1% penicillin-streptomycin (Gibco, USA). The primary cells were cultured at 37 °C in 5% CO_2, with the medium changed every 2–3 days. Spindle-shaped cells from passage 4 or earlier were utilized for the in vitro cell experiments. The RAW264.7 cell line was obtained from the Cell Bank of the Chinese Academy of Sciences, Shanghai, China.

Cell Viability Assay: The tenocytes were seeded uniformly into 96-well plates and cultured until they reached a density greater than 90%. Thereafter, the cells were treated with different concentrations of RuO_2 for 24 h. Cell viability was assessed using the CCK-8 assay (Dojindo, Japan). The experiment was repeated 6 times ($n = 6$), and the data were presented as the mean values. The same method was used to evaluate the viability of RAW264.7 cells.

AM/PI Staining: First-generation tenocytes were seeded in a 24-well plate, and when the cell density reached 90%, they were treated with different concentrations of RuO_2 for 24 h. After PBS washing, a pre-prepared AM/PI staining solution (Beyotime, China) was added, and the tenocytes were co-incubated in a dark environment for 30 min, followed by observation under a fluorescence microscope. The same method was used to perform calcein-AM/PI staining on RAW264.7 cells.

Phalloidin Staining: First-generation tenocytes were seeded in a 24-well plate, and when the cell density reached 90%, they were treated with different concentrations of RuO_2 for 24 h. After PBS washing, the cells were fixed with 4% paraformaldehyde at room temperature for 15 min. Following PBS washing, the cells were incubated with 0.3% Triton X-100 (SaiGuo, China) at room temperature for 15 min. After another PBS wash, the cells were stained with pre-prepared Actin-Tracker Green-488 (Beyotime, China) in a dark environment for 30 min. The Actin-Tracker Green-488 was then removed, and the cells were stained with DAPI (Abcam, UK). After 1 h, the cells were observed under a fluorescence microscope. The same method was used to perform phalloidin staining on RAW264.7 cells.

IF Analysis: First-generation tenocytes were seeded in a 24-well plate, and when the cell's density reached 90%, they were treated with TBHP or RuO_2 for 4 h. After PBS washing, the cells were fixed with 4% paraformaldehyde for 15 min and permeabilized with 0.3% Triton X-100 for 15 min. The cells were then washed with PBS, blocked with 5% bovine serum albumin (BSA) at room temperature for 1 h, and incubated with primary antibody diluted in 1% BSA at 4 °C overnight. The primary antibodies used were: Col1a1 (A16891, ABclonal, China), and Col3a1 (M00788, Boster, USA). Subsequently, the cells were stained with FITC-conjugated anti-rabbit antibody (Invitrogen, USA) at room temperature in the dark for 1 h, followed by DAPI counterstaining for 1 h. Images were acquired using a fluorescence microscope (Zeiss, Germany). Fluorescence intensity was analyzed using Image J (USA, version 1.8.0) as described previously.[41] The same staining method was used for tissue samples.

Western Blotting of Protein Expression: After different treatments, the tenocytes were washed once with PBS. Total cellular proteins were extracted using RIPA Lysis Buffer (Solarbio, China) containing a protease and phosphatase inhibitor cocktail (Solarbio, China). The protein concentration was determined using the Quick Start Bradford 1× Dye Reagent (Bio-Rad, USA) after centrifugation. Equal amounts of protein samples were separated using the Omni-Easy One-step PAGE Gel Fast Reserve Kit (Epizyme, China) and then transferred to a polyvinylidene fluoride (PVDF) membrane (Sigma-Aldrich, USA). The PVDF was blocked with 5% milk (Biofroxx, Germany) at room temperature for 1 h and then incubated with primary antibodies at 4 °C overnight. The primary antibodies used were: Col1a1 (A16891, ABclonal, China), Col3a1 (M00788, Boster, USA), Mmp13 (GB11247-1-100, Servicebio, China), Cox2 (12282, Cell Signaling Technology, USA), Gpx4 (ab125066, Abcam, UK), Fth1 (4393, Cell Signaling Technology, USA), β-actin (4967, Cell Signaling Technology, USA). Horseradish peroxidase-conjugated goat anti-rabbit/mouse IgG (Biosharp, China) was used as the secondary antibody. Images were captured using a western blotting imaging system (Tanon, China), and the protein quantification was performed using Image J (USA, version 1.8.0).

qPCR: Total RNA was extracted from the tenocytes after different treatments using the RNA-quick Purification Kit (ES Science, China) according to the manufacturer's instructions. qPCR was performed on a Light Cycler 480 PCR System (Roche, Switzerland) using the SYBR Green Q-PCR Kit (Vazyme, China). The primer sequences used are shown in Table S1 (Supporting Information).

Intracellular Lipid Peroxidation, ROS, and Fe^{2+} Detection: The levels of intracellular lipid peroxidation, ROS, and Fe^{2+} were measured using fluorescence microscopy as described previously.[42] Briefly, the tenocytes after 4 h of different treatments were incubated with 5 µM lipid peroxidation probe C11BODIPY 581/591 (GC40165, GLPBIO, USA), 10 µM ROS probe DCFH-DA (S0033S, Beyotime, China), and 1 µM Fe^{2+} probe FerroOrange (F374, Dojindo, Japan) in the incubator (37 °C, 5% CO_2) for 30 min, respectively. The cells were then observed under a fluorescence microscope, and the fluorescence intensity was quantified using Image J (USA, version 1.8.0).

Statistical Analysis: Statistical analysis was performed using GraphPad Prism 8.0 (version 8.0) software. All experiments were repeated at least three times. One-way analysis of variance (ANOVA) was conducted to assess the statistical differences among the means of multiple groups. The data were presented as mean ± SD, and $P < 0.05$ was considered statistically significant. (* $P < 0.05$, ** $P < 0.01$), and ns denotes no significance.

Supporting Information

Supporting Information is available from the Wiley Online Library or from the author.

Acknowledgements

C.Q., Z.S., and F.M. contributed equally to this work. This research was funded by the Scientific Research Project of Jiangsu Commission of Health (LKZ2022011), Jiangsu Funding Program for Excellent Postdoctoral Talent (2022ZB744, 2022ZB753), China Postdoctoral Science Foundation (2022M723892, 2023M734292), the National Science Foundation of China (82172481).

Conflict of Interest

The authors declare no conflict of interest.

Data Availability Statement

The data that support the findings of this study are available from the corresponding author upon reasonable request.

Keywords

antioxidant nanozyme, ferroptosis, reactive oxygen species, ruthenium oxide, tendinopathy

Received: February 25, 2025
Revised: May 28, 2025

[1] S. de Jonge, C. van den Berg, R. J. de Vos, H. J. van der Heide, A. Weir, J. A. Verhaar, S. M. Bierma-Zeinstra, J. L. Tol, *Br. J. Sports Med.* **2011**, *45*, 1026.

[2] C. Hopkins, S. C. Fu, E. Chua, X. Hu, C. Rolf, V. M. Mattila, L. Qin, P. S. Yung, K. M. Chan, *Asia Pac. J. Sports Med. Arthrosc. Rehabil. Technol.* **2016**, *4*, 9.

[3] X. D. Miao, H. F. Jiang, Y. P. Wu, H. M. Tao, D. S. Yang, H. Hu, *J. Foot Ankle Surg.* **2016**, *55*, 529.
[4] J. K. G. Louwerens, H. Alkaduhimi, M. P. J. van den Bekerom, *Arthroscopy* **2020**, *36*, 625.
[5] T. de Zordo, N. Ahmad, F. Ødegaard, M. T. Girtler, W. Jaschke, A. S. Klauser, R. K. Chhem, C. Romagnoli, *Ultraschall Med.* **2011**, *32*, 117.
[6] S. P. Magnusson, H. Langberg, M. Kjaer, *Nat. Rev. Rheumatol.* **2010**, *6*, 262.
[7] T. P. Vo, G. W. K. Ho, J. Andrea, *Curr. Sports Med. Rep.* **2021**, *20*, 453.
[8] G. A. Murrell, *J. Shoulder Elbow Surg.* **2007**, *16*, S208.
[9] N. L. Millar, G. A. C. Murrell, I. B. McInnes, *Rheumatology* **2013**, *52*, 769.
[10] C. S. Bestwick, N. Maffulli, *Br. J. Sports Med.* **2004**, *38*, 672.
[11] N. L. Millar, G. A. Murrell, I. B. McInnes, *Nat. Rev. Rheumatol.* **2017**, *13*, 110.
[12] P. P. Y. Lui, X. Zhang, S. Y. Yao, H. N. Sun, C. H. Huang, *Int. J. Mol. Sci.* **2022**, *23*, 3571.
[13] K. Q. Li, Y. Deng, G. M. Deng, P. Y. Chen, Y. T. Wang, H. T. Wu, Z. G. Ji, Z. L. Yao, X. R. Zhang, B. Yu, K. R. Zhang, *Stem Cell Res. Ther.* **2020**, *11*, 131.
[14] H. T. Shen, L. X. Cheng, Q. Q. Zheng, W. D. Liu, Y. Wang, *Acta Biomater.* **2022**, *152*, 440.
[15] S. J. Dixon, K. M. Lemberg, M. R. Lamprecht, R. Skouta, E. M. Zaitsev, C. E. Gleason, D. N. Patel, A. J. Bauer, A. M. Cantley, W. S. Yang, B. Morrison, B. R. Stockwell, *Cell* **2012**, *149*, 1060.
[16] D. L. Tang, X. Chen, R. Kang, G. Kroemer, *Cell Res.* **2021**, *31*, 107.
[17] X. J. Jiang, B. R. Stockwell, M. Conrad, *Nat. Rev. Mol. Cell Biol.* **2021**, *22*, 266.
[18] D. L. Tang, G. Kroemer, *Curr. Biol.* **2020**, *30*, R1292.
[19] X. Y. Li, P. Fang, J. T. Mai, E. T. Choi, H. Wang, X. F. Yang, *J. Hematol. Oncol.* **2013**, *6*, 19.
[20] J. Yao, Y. Cheng, M. Zhou, S. Zhao, S. C. Lin, X. Y. Wang, J. J. X. Wu, S. R. Li, H. Wei, *Chem. Sci.* **2018**, *9*, 2927.
[21] K. Jomova, S. Y. Alomar, S. H. Alwasel, E. Nepovimova, K. Kuca, M. Valko, *Arch. Toxicol.* **2024**, *98*, 1323.
[22] Y. M. Sun, S. D. Mu, Z. Y. Xing, J. S. Guo, Z. H. Wu, F. Y. Yu, M. R. Bai, X. L. Han, C. Cheng, L. Ye, *Adv. Mater.* **2022**, *34*, 2206208.
[23] F. Muhammad, X. W. Chen, J. Y. Tang, Y. Cheng, Y. Y. Li, C. X. Zhu, Y. H. Zhang, L. Y. Miao, Y. Deng, H. Wei, *Chem. Sci.* **2024**, *15*, 1679.
[24] Z. Y. Sun, F. Muhammad, C. F. Qiao, W. L. Gong, Z. Wang, Y. Liu, X. Yu, J. Dong, J. Lv, X. Cheng, Z. H. Lu, C. G. Lin, Z. Y. Lv, W. S. Sun, T. Yuan, J. Meng, R. Wu, D. Q. Shi, H. Wei, N. R. Bao, *Small* **2025**, *21*, 2406210.
[25] H. J. Kwon, D. Kim, K. Seo, Y. G. Kim, S. I. Han, T. Kang, M. Soh, T. Hyeon, *Angew. Chem., Int. Ed.* **2018**, *57*, 9408.
[26] A. D'Addona, N. Maffulli, S. Formisano, D. Rosa, *Surgeon* **2017**, *15*, 297.
[27] J. Y. Sunwoo, C. D. Eliasberg, C. B. Carballo, S. A. Rodeo, *J. Orthop. Res.* **2020**, *38*, 1666.
[28] H. Liu, J. Y. Xu, Y. Lan, H. W. Lim, R. L. Jiang, *Front. Cell Dev. Biol.* **2021**, *9*, 654397.
[29] H. H. Liu, C. Zhang, S. A. Zhu, P. Lu, T. Zhu, X. N. Gong, Z. W. Zhang, J. J. Hu, Z. Yin, B. C. Heng, X. Chen, H. W. Ouyang, *Stem Cells* **2015**, *33*, 443.
[30] J. Y. Cai, J. Liu, J. J. Xu, Y. F. Li, T. Zheng, T. L. Zhang, K. Han, S. J. Chen, J. Jiang, S. H. Wu, J. Z. Zhao, *Biofabrication* **2023**, *15*, 025002.
[31] X. Q. Xu, R. L. Wang, Y. X. Li, R. Wu, W. J. Yan, S. Zhao, Q. Y. Liu, Y. Du, W. L. Gong, W. T. Li, H. Wei, D. Q. Shi, *Nano Res.* **2023**, *16*, 7364.
[32] J. Wang, K. Pantopoulos, *Biochem. J.* **2011**, *434*, 365.
[33] S. Yang, T. Y. Zhang, Y. L. Ge, Y. P. Cheng, L. H. Yin, Y. P. Pu, Z. Z. Chen, G. L. Liang, *ACS Nano* **2023**, *17*, 24988.
[34] H. Q. Hu, S. Y. Hua, X. H. Lin, F. Lu, W. T. Zhang, L. H. Zhou, J. R. Cui, R. X. Wang, J. Y. Xia, F. Xu, X. Y. Chen, M. Zhou, *ACS Nano* **2023**, *17*, 11692.
[35] Y. Gao, M. Tong, T. L. Wong, K. Y. Ng, Y. N. Xie, Z. W. Wang, H. J. Yu, J. J. Loh, M. Li, S. Ma, *ACS Nano* **2023**, *17*, 22240.
[36] H. Heydari, S. E. Moosavifard, S. Elyasi, M. Shahraki, *Appl. Surf. Sci.* **2017**, *394*, 425.
[37] N. Singh, M. A. Savanur, S. Srivastava, P. D'Silva, G. Mugesh, *Angew. Chem., Int. Ed.* **2017**, *56*, 14267.
[38] Y. M. Zhang, L. X. Feng, W. T. Zhan, S. J. Li, Y. L. Li, X. Z. Ren, P. X. Zhang, L. N. Sun, *ACS Appl. Energy Mater.* **2020**, *3*, 4014.
[39] W. Liu, T. Deng, L. J. Feng, A. Xie, J. C. Zhang, S. P. Wang, X. F. Liu, Y. Z. Yang, J. X. Guo, *CrystEngComm* **2015**, *17*, 4850.
[40] E. S. Trevisan, C. C. S. Martignago, L. Assis, J. C. Tarocco, S. Salman, L. dos Santos, R. Liebano, C. R. Tim, *Am. J. Phys. Med. Rehabil.* **2020**, *99*, 725.
[41] G. G. Farías, C. M. Guardia, D. J. Britt, X. L. Guo, J. S. Bonifacino, *Cell Rep.* **2015**, *13*, 1221.
[42] X. Deng, T. Z. Liu, Y. T. Zhu, J. F. Chen, Z. Song, Z. P. Shi, H. R. Chen, *Bioact. Mater.* **2024**, *33*, 483.